Volume 7 | Number 37 | 7 October 2016 | Pages 5741–5890

Polymer Chemistry

www.rsc.org/polymers

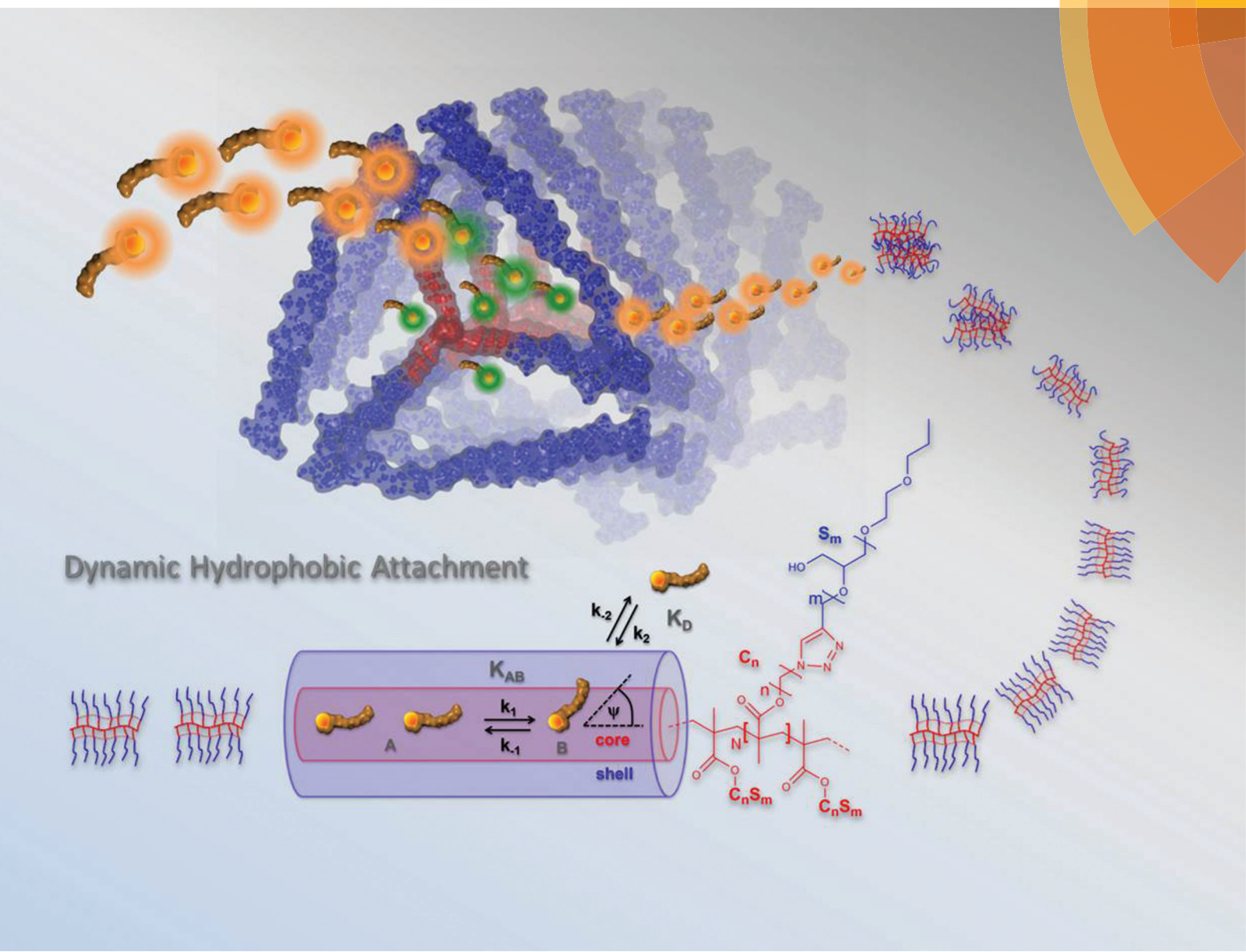

ISSN 1759-9954

ROYAL SOCIETY OF CHEMISTRY

PAPER
Dariush Hinderberger *et al.*
Tunable dynamic hydrophobic attachment of guest molecules in amphiphilic core–shell polymers

175 YEARS

Polymer Chemistry

PAPER

View Article Online
View Journal | View Issue

Cite this: *Polym. Chem.*, 2016, **7**, 5783

Tunable dynamic hydrophobic attachment of guest molecules in amphiphilic core–shell polymers†

Jörg Reichenwallner,[a] Anja Thomas,[b] Lutz Nuhn,[b,c] Tobias Johann,[b] Annette Meister,[a,d] Holger Frey[b] and Dariush Hinderberger*[a]

Received 30th July 2016,
Accepted 23rd August 2016

DOI: 10.1039/c6py01335j

www.rsc.org/polymers

In this study, synthesis and dynamic properties of amphiphilic core–shell polymers are reported as monitored through their interaction with small amphiphilic molecules. Brush-like structures are formed with a hydrophobic core surrounded by a hydrophilic shell utilizing controlled radical addition–fragmentation chain transfer (RAFT) polymerization of macromonomers consisting of linear polyglycerol chains attached to alkylene methacrylate. Continuous wave electron paramagnetic resonance (CW EPR) spectroscopy is employed to study how the amphiphilic, paramagnetic spin probe 16-DSA (16-doxyl stearic acid) interacts with polymers of different alkylene chain lengths in their hydrophobic cores and different polyglycerol chain lengths in their hydrophilic shells. The spin probe exhibits dynamic hydrophobic attachment to the polymers and reveals an indirect, dynamics-based view of polymer effects such as temperature response, aggregation and ligand binding properties. Increasing the hydrophobic alkylene chain length in the polymers alters the physical properties of the core region significantly. A large set of controllable functional polymer properties can be adjusted by the degree of polymerization and alkylene spacer length. Partial aggregation of the polymers further modifies the binding properties. Applying dynamic light scattering (DLS), transmission electron microscopy (TEM) and molecular dynamic (MD) simulations, the complex dynamic behavior found with EPR spectroscopy was further complemented and verified.

1. Introduction

In recent years, synthetic pathways have been established to construct graft copolymers from amphiphilic macromonomers[1–8] with high molecular weights of up to 470 kDa and narrow and monomodal weight distributions (PDI < 1.20).[9] Therefore, these polymers are especially well suited for the design of specialized and reproducible functional properties in the realm of smart materials,[10–13] *e.g.*, employing their capabilities to host small ligand molecules in their hydrophobic core.[14–17]

One method to monitor ligand uptake is to chemically attach paramagnetic nitroxide moieties as spin labels to the ligands, which makes them amenable to electron paramagnetic resonance (EPR) spectroscopic investigations. A standard biological example for the case of fatty acid uptake is the major blood transport protein albumin, whose ligand uptake capabilities are mainly driven by thermodynamics, by electrostatic and hydrophobic (entropic) forces.[18] So far, EPR spectroscopy has contributed substantial information about the mutual interactions of this biomacromolecule with spin-labeled fatty acids, specifically doxyl stearic acids (see Fig. 1),[19–24] and has indirectly provided a profound basis for functional analysis that will be applied in this study. Furthermore, it has been shown that albumin fatty acid binding capacities can be modulated artificially by post-translational surface modifications, aiming for both, an increased[25] or a decreased ligand uptake capacity.[26]

From a synthetic point of view, charged dendronized polymers have already been reported as fatty acid transporters whose uptake capabilities scale exponentially with the dendrimer generation.[27] In principle, this shows that it is possible to tune ligand uptake capabilities by chemical modification of polymeric building blocks. Additionally, upon application of external stimuli such as pH,[28] ionic liquids, salt,[27] light[16] or temperature the bound fatty acid ligands can also be released selectively, *e.g.* in Poloxamers[29] (= Pluronics) or elastin-like polypeptides[28] (ELPs).

[a]*Institute of Chemistry, Martin-Luther-Universität Halle-Wittenberg, Von-Danckelmann-Platz 4, 06120 Halle, Germany. E-mail: dariush.hinderberger@chemie.uni-halle.de*
[b]*Institute of Organic Chemistry, Johannes Gutenberg-University, Duesbergweg 10-14, 55128 Mainz, Germany*
[c]*Department of Pharmaceutics, Ghent University, Ottergemsesteenweg 460, 9000 Ghent, Belgium*
[d]*Institute of Biochemistry and Biotechnology, Martin-Luther-Universität Halle-Wittenberg, Kurt-Mothes-Straße 3, 06120 Halle, Germany*

† Electronic supplementary information (ESI) available: Details on synthesis and physical characterization, as explained in the text. See DOI: 10.1039/c6py01335j

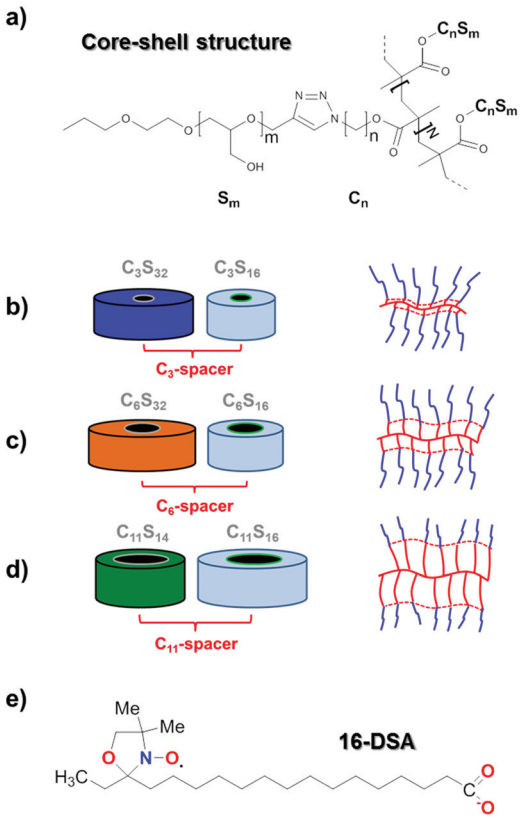

Fig. 1 Composition of all six core–shell polymers C_nS_m. (a) Generalized chemical structure of a core–shell polymer with *N* macromonomer repeating units consisting of *m* glycerol and *n* methylene components. (b) Propylene spacer polymers C_3S_{32} (blue) and C_3S_{16} (pale blue). (c) Hexylene spacer polymers C_6S_{32} (orange) and C_6S_{16} (pale blue). (d) Undecanoylene spacer polymers $C_{11}S_{14}$ (green) and $C_{11}S_{16}$ (pale blue). On the left hand scheme in (b), (c), and (d), the individual polymers are schematically color coded as they will appear in our subsequent analysis. A brush-like representation of the polymers is also given on the right hand side of (b)–(d) highlighting the hydrophobic core (red) and shell region (blue). The pale blue polymers are all equipped with a S_{16} shell. (e) Chemical structure of the 16-DSA spin probe.

Spectroscopically, we can study paramagnetic fatty acids by continuous wave (CW) EPR to determine their distribution in different environments based on polarity and their individual binding affinities as well as partition coefficients. The two major reference points are the free (*f*) and strongly bound and immobilized (*b*) spectral fractions that can easily be separated by their spectral shape and therefore facilitate extraction of valuable dynamic information (see Fig. 2). The basis for this spectral separation is the lineshape broadening upon decelerated diffusion.[30–34] Freely tumbling fatty acid ligands exhibit typical isotropic three line EPR spectra, with well-defined solvent-specific line splittings (a_{iso}) as it is commonly encountered for fast rotating nitroxide radicals with rotational correlation times τ_c of about 10–500 ps. Upon binding to a macromolecular substrate such as a polymer or a protein, the rotational motion is slowed down about three orders of magnitude to the ns-timescale, as it then reflects the slower rotational motion of the corresponding macromolecular structure (τ_c > 0.5 ns).[34,35] Then, broad anisotropic EPR lineshapes are observed that are dominated by the shape, size and polarity of the macromolecular environment. As a nonpolar environment leads to a local shift of the electron spin density towards the oxygen atom in nitroxide radicals, the hyperfine interactions between electron and ^{14}N nucleus and hence the a_{iso}-value is reduced linearly with decreasing polarity.[36,37] Thus, the spectral parameters, *i.e.*, the individual dynamic fractions *f* and *b*, as well as τ_c and a_{iso}, are the key to dissecting multicomponent EPR spectra. This forms the foundation of our approach of detecting structural and dynamic changes of the polymer itself, extending the established phenomenon of merely observing ligand binding towards polymers.[14,16,17]

Furthermore, structural and dynamical aspects are complemented by dynamic light scattering (DLS), transmission electron microscopy (TEM) and molecular dynamics (MD) simulations, giving additional resolution of different dynamic processes on the nanoscopic scale. We will in the following show that our deliberate physico-chemical, EPR-based strategic approach can lead to an almost holistic view of how macromolecular structure and dynamic responses can be tuned.

2. Results and discussion

2.1 Polymer synthesis and screening by EPR spectroscopy

In this study, we characterize different amphiphilic core–shell polymers, in which parameters like the degree of polymerization (*N*) of the polymethacrylate backbone, but particularly the length of hydrophilic linear polyglycerol shells (*lin*PPG_m, in short denoted as S_m) and alkylene core spacer lengths (in short denoted as C_n) are varied. As a simplification all polymers will be denominated with a distinctive abbreviation C_nS_m according to their structural composition. The chemical rationale of all macromonomers is given in Fig. 1a with respect to its most important tunable entities (*m*, *n*), also highlighting the chemical structure of the polymethacrylate backbone comprising *N* subunits. In Fig. 1b–d a schematic representation of all core–shell polymers is given in a cylindrical and brush-like representation. All polymers were synthesized by radical addition–fragmentation chain transfer (RAFT) polymerization, a controlled polymerization technique, that provides well-defined (block co-)polymer architectures with narrow molecular weight distributions and precisely defined α- and ω-end-functionalities.[38–40] To the best of our knowledge, the grafting through polymerization of polyglycerol-based macromonomers by RAFT leading to well-defined end-functional graft copolymers has not been described in the literature to date. We succeeded in synthesizing the amphiphilic polyglycerol-based macromonomers by clicking azido alkyl methacrylates of different spacer lengths (propylene = C_3, hexylene = C_6, undecanoylene = C_{11}) to the propargyl-functional *lin*PPG_m in a copper-catalyzed azide–alkyne cycloaddition (CuAAC). While the synthesis of C_3 and C_6-based core–shell polymers has been reported before,[9] the longer undecanoylene spacer has not been employed up to now. Using (4-cyanopentanoic

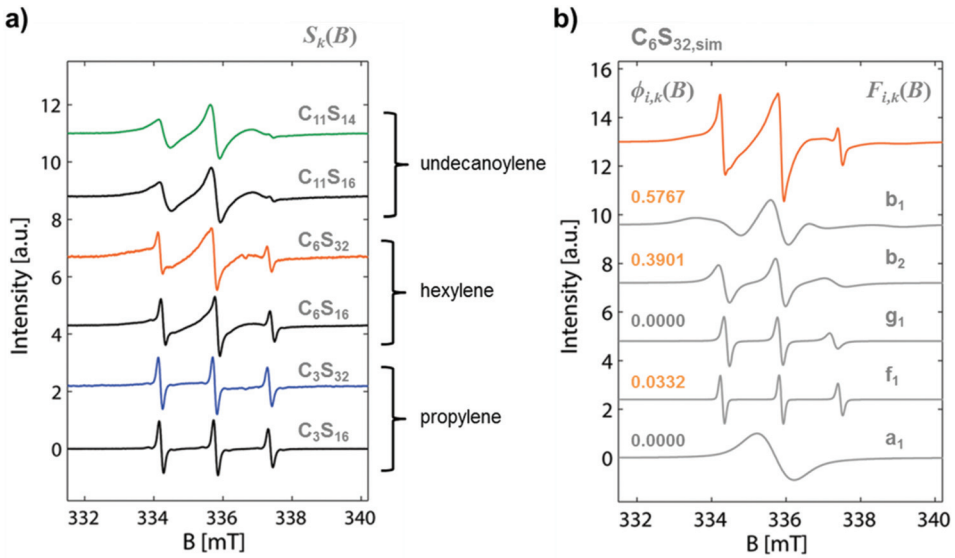

Fig. 2 Collection of CW EPR spectra of different amphiphilic core–shell polymers as probed with 16-DSA at T = 25 °C. (a) Summary of EPR spectra $S_k(B)$ from polymers with propylene (C_3), hexylene (C_6) and undecanoylene (C_{11}) spacers. (b) Representative simulation of polymer $C_6S_{32,sim}$ (orange) composed of an overlay of three exactly balanced (see orange numbers) fractions $\phi_{i,k}(B)$ of dynamic components $F_{i,k}(B)$ in this case being b_1, b_2 and f_1 (compare to a). The components a_1 and g_1 are also shown for completeness. All simulation traces are shown in grey. Measurements were conducted in H_2O at concentrations of 1 wt% (C_3) and 4 wt% (C_6 and C_{11}) and a 16-DSA concentration of about 200 μM.

acid)dithiobenzoate as charge transfer agent for the RAFT polymerization, well-defined core–shell polymers of narrow polydispersity are accessible that can even further be modified towards heterotelechelic graft copolymers with reductive cleavable or non-cleavable fluorescent end groups. Details on synthesis and characterization summarized in the Experimental section and in the ESI† demonstrate the versatility of RAFT polymerization conditions for amphiphilic polyglycerol-based macromonomers towards well-defined end-functional core–shell polymers.

For analysis of the dynamic properties of the polymers, we chose the amphiphilic spin probe 16-DSA[41,42] to monitor the microenvironment of the polymer solutions and potential binding to the polymers by means of EPR spectroscopy.[28,43] The chemical structure of 16-DSA is given in Fig. 1e.

The advantage of using this spin probe is the rigid attachment of the nitroxide moiety to the alkyl chain, so that the change in motional freedom of this long chain (C_{18}) is directly and accurately reflected in an EPR spectrum.[41,44] In Fig. 2a, CW EPR spectra of 16-DSA co-dissolved in solutions of all available core–shell polymers are shown. Interestingly, the overall spectral shape evidently only changes significantly with alkylene spacer length C_n, clearly indicating an affinity-based variation in the ratio of free (f) to bound (b) ligand due to the hydrophobic core. In the following we present data for one representative polymer from each group of similar alkylene spacer lengths: C_3S_{32}, C_6S_{32}, and $C_{11}S_{14}$. This selection allows studying the effect of short alkylene spacers shielded by a thick hydrophilic shell (C_3S_{32} and C_6S_{32}) and long alkylene spacers shielded by a much thinner hydrophilic layer ($C_{11}S_{14}$), so that we can observe the maximum number of individual effects of structural properties (spacer length, shell thickness and degree of polymerization) on the ligand binding and conformational changes while keeping the number of datasets at a manageable level.

The studied polymers are color coded as in Fig. 1b–d throughout the whole manuscript. All important polymer data such as molecular weight (MW), macromonomer weight (MW_{MM}), polydispersity index of the macromonomer (PDI_{MM}), and degree of polymerization (N) can be found in Table 1.

From an EPR spectroscopic point of view, we encounter experimental spectra that are composed of a set of five distinguishable sub-spectra $F_{i,k}(B)$ resembling different spin probe dynamic regimes and environments as seen in Fig. 2b. We will later show that these different rotational and environmental regimes correspond to different topologies and mobilities in the three different core–shell polymer solutions. The index i denotes the type of sub-spectrum and k denotes the individual polymer sample. The according spectral components can be extracted from rigorous simulations of experimental EPR spectra. Upon addition of the 16-DSA spin probe to the polymer solution, we find 16-DSA as a freely tumbling

Table 1 Properties of C_nS_m polymers

Polymer	n	m	MW [kDa]	MW_{MM} [kDa]	N	PDI_{MM}
C_3S_{32} [a]	3	32	100	2.68	37.3	1.07
C_6S_{32} [a]	6	32	470	2.72	172.8	1.11
$C_{11}S_{14}$ [b]	11	14	64.3	1.46	44.0	1.25

[a] From ref. 9. [b] This work.

species (f_1), a species aggregated in micelles (a_1, as the stearic acid spin probes have a critical micellar concentration of about 0.3 mM in phosphate buffered saline at pH 7.4),[45] a slowly tumbling species (b_1), an intermediately slow tumbling species (b_2) and it also appears in a gel phase (g_1) very similar to the hydrogels described in Junk *et al.*[46] The respective spectral fractions of all species are given by $\phi_{i,k}$. In principle, any occurring experimental spectrum $S_k(B)$ can be reconstructed by the formal relation $S_k(B) = \sum \phi_{i,k} \cdot \iint F_{i,k}(B)$ where $\sum \phi_{i,k} = 1$ (see Fig. 2b). Further explicit information about the simulations and reconstruction technicalities of experimental spectra can be found in the ESI.† All spectra from C_6- and C_{11}-polymer-solutions show distinct, broad spectral lines stemming from strong spin probe immobilization upon binding and overlapping of different dynamical regimes. While C_6- and C_{11}-type polymers show 16-DSA spectra exclusively composed of b_1, b_2, and f_1, we show that C_3S_{32} and C_3S_{16} exhibit three line spectra resembling freely tumbling 16-DSA and C_3S_{32} may comprise small fractions of f_1, g_1 and a_1. The shape and relative fractions of these spectral components will be used for subsequent analysis.

2.2. Temperature dependence of ligand binding

The so-called hydrophobic effect is a driving force of ligand binding to macromolecules and is strongly dependent on temperature.[47,48] Hence, we conducted temperature-dependent EPR measurements of the solutions to obtain the dynamic response of the polymers *via* their modulated interaction with the 16-DSA spin probe. As a reference, we investigated the temperature response of 16-DSA alone without polymer and found that neither micellization nor any phase transitions occur in the whole temperature range (see Fig. S1 and S2†). As the evaluation of a multicomponent EPR spectrum at a single temperature always suffers from a potential inseparability of the individual spectral components, measuring a temperature series may unravel all dynamic regimes, as the individual fractions have different temperature dependences and can thus be individually discerned and investigated in detail. In case of the polymers available, this strategy proved successful yet exceptionally complicated, as sub-spectra separation had to be conducted iteratively in a manual global fit. Ultimately, the results from spectral simulations of temperature-dependent measurements are displayed in Fig. 3a–d, where only the spectral fractions $\phi_{i,k}$ of the respective components are plotted as a function of temperature. Simulation parameters and all simulated spectra as well as the deconvolution routine can be found in the ESI in Table S1, Fig. S1 and S3–S6.† The individual 16-DSA concentrations were determined by (relative) spin counting and are shown as grey insets in Fig. 3.

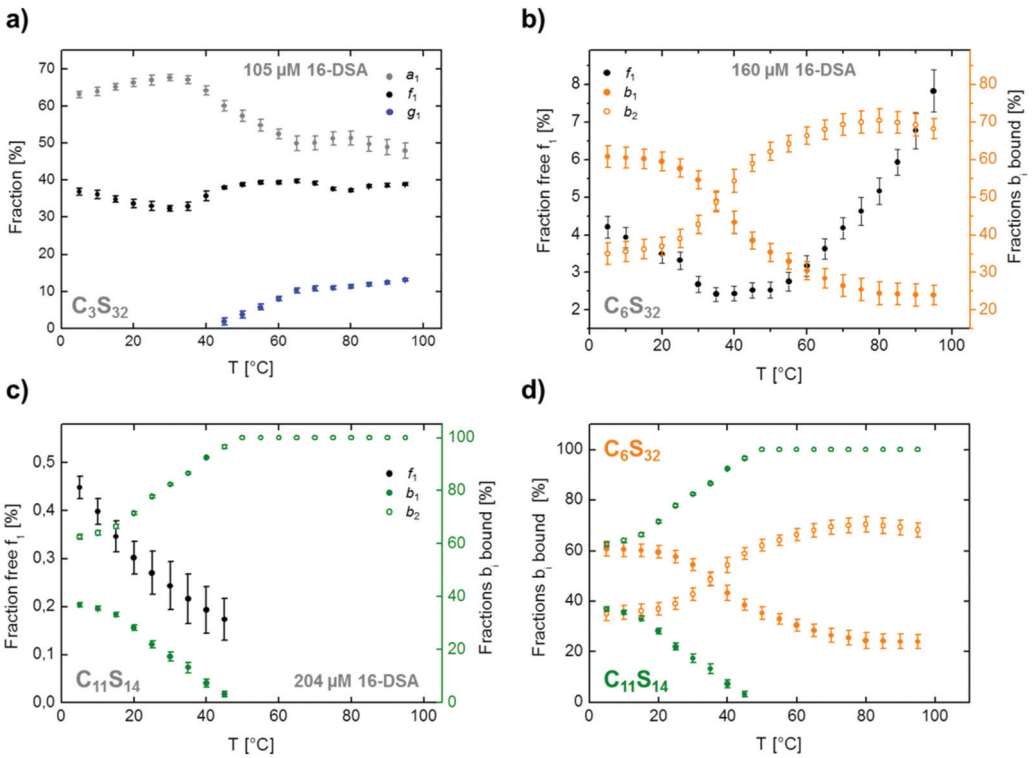

Fig. 3 Temperature response from C_nS_m core–shell polymers in the temperature range from 5–95 °C loaded with 16-DSA depicted as fractions $\phi_{i,j,k}$. (a) 1 wt% C_3S_{32} spin probed with 105 μM 16-DSA. (b) 4 wt% C_6S_{32} spin probed with 160 μM 16-DSA. (c) 4 wt% $C_{11}S_{14}$ spin probed with 204 μM 16-DSA and (d) a comparison of the slow (b_1) and intermediately slow (b_2) rotating components of C_6S_{32}- and $C_{11}S_{14}$-polymers. Micellar fractions a_1 are shown in grey, gel fractions g_1 in blue and free fractions f_1 in black throughout. The responses of polymers C_6S_{32} (orange) and $C_{11}S_{14}$ (green) can be subdivided in slow rotating (● = b_1) and intermediately slow rotating (○ = b_2) regimes. Error margins have been determined from spectral simulations.

As can be seen in Fig. 3a, the bulk of the 16-DSA molecules in the C_3S_{32} polymer solution resides in micelles or tumbles freely in solution. In the temperature range from 5–40 °C the CW EPR spectra reveal only free (f_1) and micellar (a_1) 16-DSA, with the sum of fractions $\phi_{i,j,k}$ adding up to 100%. The subscript j now extends the specificity of our spectral fractions from type of sub-spectrum (i) and polymer (k) and denotes the temperature T. The micelle fraction decreases above 40 °C giving rise to a simultaneous increase of free 16-DSA in solution, most probably by a temperature-based shift in equilibrium between micelles and free 16-DSA. Above 45 °C a third component emerges with a strongly hydrophobic/non-polar a_{iso}-value of 40.24 MHz (14.36 G) and a rotational correlation time of τ_c = 0.4–0.7 ns. This is indicative of the formation of a hydrogel-like environment by the C_3S_{32} polymer as it has been shown for thermoresponsive polymers[49–51] and is therefore denoted as the sub-spectrum g_1. A comparison with 16-DSA alone in DPBS[52] buffer shows a clear deviation in the high-field region of the EPR spectra (Fig. S4†).

The steep increase of the gel fraction is nonlinear in the observable temperature range and can be expected to be time-dependent as well. Our EPR data show that the C_3S_{32}-core–shell polymer most probably forms small hydrogel-like entities above 40 °C by forming water depleted regions which are detected by the amphiphilic spin probes, while there is no spin probe uptake at temperatures close to room temperature. Loading studies with the smaller and more hydrophilic spin probe TEMPO did not indicate any immobilization or binding in the C_3S_{32} polymer either (data not shown). The reasons for this uptake behavior are discussed in subsequent sections. One can further assume a complicated thermodynamic equilibrium in terms of competition for fatty acids between micelles and C_3S_{32} polymer.[53,54] Another interesting fact is that the emergence of large micelle fractions at such low fatty acid concentrations of 100–150 μM may indicate a polymer-induced decrease of the fatty acid solubility in aqueous solution (see Fig. S4†). In this context we have to mention that also the ionic strength of the DPBS buffer of the pure 16-DSA solution may alter the CMC towards higher values. Finally, our data show that for the C_3S_{32} polymer effective binding and transport of amphiphilic ligands like our stearic acid derivatives can be excluded at least for individual polymers at ambient conditions.

The spin probes together with the C_6S_{32}-polymer in Fig. 3b display a completely different development of dynamic regime occupations. There are three overlapping spectral components $F_{i,j,k}(B)$ in the whole temperature range (f_1, b_1, b_2). The b_1 and b_2 fractions of 16-DSA strongly interact with the polymer and hence are significantly hampered in their rotational motion (shown in orange). The sum of bound fractions $\sum\phi_{b,j,k}$ (b_1 and b_2) constantly amounts to over 92% for all temperatures without any micellar aggregates (a_1) or gels (g_1) appearing. The respective a_{iso}-value of 42.80 MHz (15.27 G) for both bound fractions b_i of C_6S_{32} indicates a much more hydrophobic environment than 44.26 MHz (15.79 G) for freely tumbling 16-DSA, giving rise to the assumption, that the spin probe is in fact in contact with the much better accessible hydrophobic and water-depleted core compared to the C_3S_{32} polymer.

The fundamental difference in fractions b_1 and b_2 is given by the rotational correlation time τ_c. At room temperature b_1 has a rotational correlation time of τ_c = 6.6 ns and b_2 has an about three times lower value of τ_c = 2.0 ns. There is a minimum free 16-DSA fraction of 2.4% around 35 °C, exactly coinciding with the crossing of the curves of slow and intermediately slow tumbling fractions, both being occupied equally at this point. Additionally, from 5 °C onwards the free fraction f decreases from 4.2% to 2.4% at 35 °C, so the fatty acid uptake can be regarded to be initially enhanced by temperature and the temperature dependent ligand uptake attains a plateau-like behavior between 35 °C and 50 °C. For temperatures exceeding 50 °C the free fraction again increases to 7.8% at 95 °C, allowing for an optimum fatty acid uptake capability in the range from 35 °C to about 50 °C, which interestingly includes the range of mammalian body temperature. Fatty acid ligand uptake of the C_6S_{32}-polymer thus clearly occurs throughout the whole temperature range.

A slightly simpler dynamic temperature response can be found for the $C_{11}S_{14}$-polymer as shown in Fig. 3c, although also exhibiting an initial simultaneous occurrence of three spectral components $F_{i,j,k}(B)$ as seen for the C_6S_{32}-polymer (f_1, b_1, b_2). The $C_{11}S_{14}$-polymer features the longest alkylene spacers in the core and we observe an almost gradual decrease of free and slow bound subspectra f_1 and b_1, both almost completely vanishing above 45 °C and leaving a single spectral component b_2 behind that can be tracked to temperatures as high as 95 °C. The corresponding a_{iso}-value of 42.44 MHz (15.14 G) for both bound fractions of the $C_{11}S_{14}$-polymer is even more hydrophobic than for the C_6S_{32}-polymer, also strongly implying contact to the hydrophobic core region. Unlike in the C_6S_{32}-polymer, here the free fraction of 16-DSA is about one order of magnitude lower, decreasing from 0.45% at 5 °C to 0.17% at 45 °C, which is a clear indication of a higher affinity of the spin probe towards the hydrophobic undecanoylene-containing core as compared to the hexylene core. The $C_{11}S_{14}$-polymer is therefore considered to have the best 16-DSA accessibility of all three polymers as the thinner hydrophilic shell reduces spatial restriction regarding ligand entry to the hydrophobic core. The rotational correlation times of the two bound fractions b_1 and b_2 at room temperature are 6.6 ns and 2.6 ns, respectively. A direct comparison with the C_6S_{32}-polymer reveals that these values are almost identical at room temperature, so the fatty acid rotational dynamics seem not to be greatly affected by the molecular weight of the polymers C_6S_{32} (470 kDa) and $C_{11}S_{14}$ (64.3 kDa). In Fig. 3d the occupation changes of both dynamic regimes b_1 and b_2 of C_6S_{32}- and $C_{11}S_{14}$ polymers are compared. This graph shows that the length of the C_n-spacer might operate as shifting the sigmoidally shaped curves (○ and ●) along the y-axis. We therefore suggest this interconversion of b_1 to b_2 with temperature to be the first tunable dynamic property of the core shell polymers, although, as it will be shown later in this manuscript, a

polymer structural correlation cannot be made from EPR data alone. The ligand uptake curves, shown in Fig. 3 in black throughout indirectly detect the optimum functional state of the polymers. The temperature dependent motional dynamics of the spin probes and polymers are summarized in Fig. 4. The rotational correlation times τ_c of all immobilized fractions b_1, b_2 and g_1 emerging from being in close contact with the polymers are depicted in Fig. 4a for the whole temperature range. In contrast to the $C_{11}S_{14}$-polymer which shows an almost linear growth of $-\log \tau_{c,j,k}$ in the semilogarithmic diagram (logarithmic decrease of τ_c) in both bound fractions b_1 and b_2, the C_6S_{32}-polymer appears to have a kinked, more *sigmoidal* temperature response of its rotational dynamics as probed by 16-DSA. This is indicative for a two-state phase transition of the polymer leading to a slightly more restricted rotational motion of the spin probe. For both, C_6S_{32} and $C_{11}S_{14}$ polymers, τ_c of the slow component b_1 decreases from 11 ns to about 2 ns from 5–95 °C, and τ_c of the intermediately slow component b_2 changes from about 3.6–5.2 ns at 5 °C to 0.40–0.47 ns at 95 °C, so the values are roughly similar and of course in the same rotational dynamic regime. As physically expected, the a_{iso}-values for f_1, b_1 and b_2 have also been found to be slightly temperature dependent and in addition are graphically summarized in Fig. S7.†

Complementing the EPR-spectroscopic temperature series, we have performed temperature-dependent DLS measurements on the samples including 16-DSA. These measurements reveal the main hydrodynamic polymer size as a function of temperature. The actual size distributions from the regularization process[55] appeared to be partly polydisperse depending on temperature and are given in Fig. S8.† While $C_{11}S_{14}$ seems to retain its main hydrodynamic size throughout the whole temperature range at about $R_{H,j,11}$ = 4 nm, the shorter alkylene chain polymers C_3S_{32} and C_6S_{32} exhibit a slightly nonlinear size behavior.

The most prominent feature of this nonlinearity is a size decrease above 25 °C from 3.5 nm to 2.6 nm for C_3S_{32} and 6.1 nm to 5.4 nm for C_6S_{32} with the minimum appearing between 33 °C and 42 °C for both polymers. This decrease in size of ΔR_H of 0.7–0.9 nm is assumed to be related to an intramolecular structural collapse most probably caused by the hydrophilic shell, as the short shell length polymer $C_{11}S_{14}$ does not show such a transition behavior. In turn, this complements our view from the EPR-derived motional restriction of

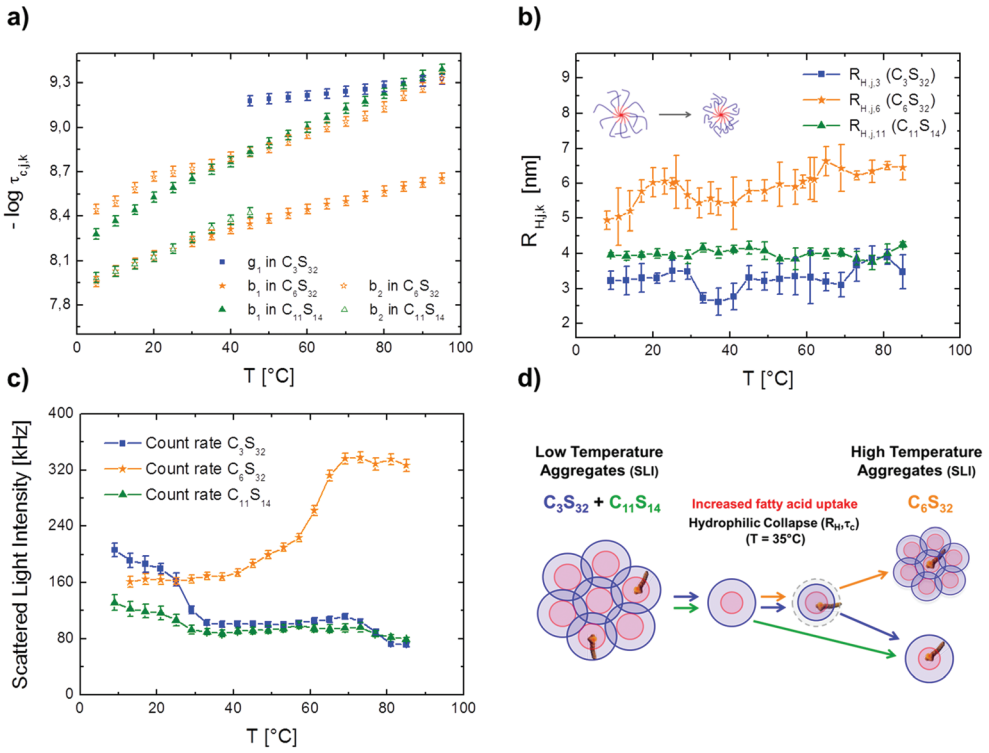

Fig. 4 Temperature-induced dynamics of spin probes and polymers. (a) Semilogarithmic plot of all emerging temperature-dependent immobilized fractions (g_1, b_1, b_2) of 16-DSA in solutions of polymers C_3S_{32}, C_6S_{32} and $C_{11}S_{14}$ as monitored by τ_c. The gel phase g_1 of the C_3S_{32}-polymer is shown in blue, the immobilized fractions b_i of the C_6S_{32}-polymer are shown in orange and $C_{11}S_{14}$-polymer fractions b_i in green. Error margins for τ_c were estimated from simulations to range about 8%. (b) Temperature dependence of the main hydrodynamic radii $R_{H,j,k}$ as detected by DLS. Error bars were calculated according to the fluctuation of individual measurements at constant temperature. (c) Scattered light intensity (SLI) given as count rates (in kHz) from temperature dependent DLS measurements of all three polymers. (d) A dynamic model for the temperature dependent formation of aggregates due to SLI of (c) in the scheme of "dynamic hydrophobic aggregation" in all three polymers based on (a)–(c) and Fig. 3. The polymer concentrations for DLS measurements were 0.13 wt% for C_3S_{32} (blue), 0.2 wt% for C_6S_{32} (orange) and 0.13 wt% for $C_{11}S_{14}$ (green).

the spin probe of the C_6S_{32} polymer with the sigmoidal $-\log \tau_{c,j,6}$ curve above 25 °C in Fig. 4a. As it can be seen from Fig. 3a and 3b, the occurrence of this minimum in solution size in Fig. 4b is correlated with a newly initiated (C_3) or increased (C_6) accessibility of the hydrophobic core for both S_{32} polymers. For the hydrophilic shell the solvent quality of water is modulated (from being a good to being a poor solvent) in this temperature range, similar to what is found for ethylene-oxide based oligomers and polymers. This in fact generates a structural breathing that will be further on denoted as *hydrophilic collapse*. This hydrophilic collapse is apparently accompanied by a modified and improved ligand uptake that can be triggered by temperature. The spin probes in the C_6S_{32} polymers experience a motional slowdown due to collapse of the formerly more water-swollen polyglycerol shell onto the hydrophobic core. As this stealth effect of the core is obviously based on the shell properties that can be modulated by synthesis, this is defined as the second dynamic tunable property.

Another clearly observable effect in the DLS measurements is the change of scattering intensity over temperature for each polymer solution (Fig. 4c). An increase in scattering intensity can generally considered to be correlated to the formation of larger particles in solution as it has been applied *e.g.* in Majhi *et al.*[56] Thus, for C_3S_{32} and $C_{11}S_{14}$ we observe dissolving low order aggregates or oligomers with increasing temperature and for C_6S_{32} aggregates form with increasing temperature (see also Fig. S8†). When inspecting the individual polymer characteristics as summarized in Table 1, it appears very likely that the temperature induced formation and depletion of aggregates is connected with the degree of polymerization N (C_6S_{32} by far has the highest N) and the aggregation probably obeys complicated thermodynamic phase transitions that are beyond the scope of this work. This behavior is considered to be the third tunable dynamic property of the core–shell polymers and will be termed as "dynamic hydrophobic aggregation". A graphical sketch of these findings is given in Fig. 4d. All results will be later rationalized in a strategic overview in section 2.7.

Another observation that can be made and analyzed upon temperature increase is that when quantitatively analyzing the absolute number of spins in the EPR data shown in Fig. 3. Besides the described extraordinary temperature behavior of different sub-spectra, these polymers seem to exhibit a mild radical scavenger property, as the double integral of the first-derivative EPR spectra (number of spin-bearing 16-DSA molecules) decreases with temperature. The scavenging mechanism apparently gets stronger as the alkylene chain length C_n increases. Therefore, it can be tentatively linked to the increased residence time τ_r with higher ligand binding affinity of the longer alkylene chains (decreasing equilibrium dissociation constant $K_D \sim 1/\tau_r$).[57] In principle, the reduction of the nitroxide moiety is assumed to follow a disproportionation reaction[58] for 16-DSA most probably similar to the thermal or acidic disproportionation reaction of the TEMPO spin probe.[43,49,59,60] This circumstance proves the realization of studies comprising polymer heating as irreversible and reliable heating-cooling cycles are therefore impossible by EPR as, *e.g.*, the $C_{11}S_{14}$ polymer depletes the spin-concentration by 80% in one heating procedure alone (2 hours). All results concerning the absolute number of spins during heating are summarized in Fig. S9,† but since we only analyze the data within the first, fast heating, for which the signal loss does not play a significant role, they are not investigated in more detail and are considered as a side effect.

2.3. Molecular dynamics (MD) simulations

Molecular dynamics simulations have the potential to add further insight to the solution behavior of the polymers. Although being purely phenomenological here a global analysis of the simulated structures gave a strong decrease of compactness of the polymers with increasing alkylene chain length. Therefore, we normalized the model radius of gyration $R_{G,M}$ to the model molecular weight MW_M giving values from 0.0362 nm kDa^{-1} for C_3S_{32}, 0.0440 nm kDa^{-1} for C_6S_{32} to 0.0580 nm kDa^{-1} for $C_{11}S_{14}$ coinciding with a slightly decreasing macromolecular density with alkylene spacer length on an empirical level. Generally, as the structure for the C_3S_{32} polymer appears to be almost globular, the $C_{11}S_{14}$ structure is more sheet-like accompanied with a qualitatively decreasing diameter. The polyglycerol chains in the periphery of the core–shell polymers appear to be rather curled and irregular (Fig. S10†). From this viewpoint the polymer brushes can therefore only be seen as strictly globular (C_3) or cylindrical in shape (C_6 and C_{11}) on short length scales only, of course depending on the degree of polymerization N and alkylene spacer length C_n. Further details from MD simulations are given in Table S2.†

2.4. Ligand uptake capabilities

Going beyond the temperature dependence of ligand uptake of the core–shell polymers, we conducted a loading study to determine the ligand binding capacities and corresponding binding affinities of all polymers at room temperature. As only C_6S_{32} and $C_{11}S_{14}$ polymers bind 16-DSA at ambient conditions, the C_3S_{32} polymer is excluded from this study. To this end, we utilize the common strategy to increase the amount of ligand in about equidistant concentration steps while keeping the polymer concentration constant. The essential parameters (f and b) can be directly assessed from simulations of EPR spectra. If the ratio of bound to free ligand varies, we can construct Scatchard plots[61–64] as a linear transformation of loading data, commonly conducted for proteins but also suitable for polymers.[65] Particularly in case of EPR spectroscopy utilizing 16-DSA as a spin probe there are abundant loading studies of the blood transport protein albumin.[19,21,23] Applying the Scatchard formula:

$$\frac{[L]_b}{[L]_f} = \frac{[L] - [L]_f}{[L]_f} = -\frac{1}{K_{D,k}}([L]_b - [L]_{b,y=0}) \quad (1)$$

to our spin probe-binding polymers, with $[L]_b$ as the concentration of bound ligand, $[L]_f$ being the concentration of free

ligand, [L] the overall concentration of used ligand, $K_{D,k}$ is the macroscopic equilibrium dissociation constant of polymer k and $[L]_{b,y=0}$ the intercept with the x-axis, we can simplify eqn (1) for our needs:

$$\nu = -\frac{1}{K_{D,k}}(N_L - N_{L,k}) \quad (2)$$

with $\nu = [L]_b/([L]_f \times [P]_k \times N)$ to directly extract the maximum number of binding sites $N_{L,k}$ of the polymer or the binding sites $N_{L,MM,k}$ of a single macromonomer. Furthermore, the relation $N_{L,MM,k} = [L]_{b,y=0}/([P]_k \times N)$ holds where $[P]_k$ is the total core–shell polymer concentration of polymer k and N is the degree of polymerization (Table 1). The results from the Scatchard plot evaluations can be found in Fig. 5 and Table 2. Furthermore, all according spectral simulations for extraction of parameters used in eqn (1) and (2) can be found in Fig. S11† and are based on the set of parameters as given in Table S1.†

The linearity observed in both Scatchard plots is generally correlated with unspecific binding to equivalent binding sites.[61] The change in the $K_{D,k}$ values upon increasing the hydrophobic alkylene chain length from C_6 to C_{11} is accompanied by a decrease of more than one order of magnitude from $K_{D,6}$ = 28.82 μM to $K_{D,11}$ = 2.42 μM, so the ligand binding is much stronger for $C_{11}S_{14}$ due to the better accessibility of the hydrophobic core. The strong decrease of $K_{D,k}$ upon increased alkylene spacer length is the fourth dynamical tunable quantity. An astonishing finding is that regarding the maximum number of binding sites $N_{L,MM,k}$ per macromonomer the C_6 polymer surpasses the C_{11} polymer slightly: a maximum number of macromonomer ligand binding sites of $N_{L,MM,6}$ = 0.0684 is found for C_6S_{32} compared to $N_{L,MM,11}$ = 0.0445 for $C_{11}S_{14}$. The reason for this fact may be connected to the partial aggregation of the $C_{11}S_{14}$ polymer at room temperature and subsequent spatial restrictions to binding sites in the hydrophobic core, whereas C_6S_{32} is mainly monomeric as obtained from our DLS data (Fig. 4c). The actual fatty acid capacity per polymer chain is clearly much higher for C_6S_{32} with $N_{L,6}$ = 11.82 than for $C_{11}S_{14}$ with $N_{L,11}$ = 1.96 as derived from Fig. 5 (see also Table 2). The straightforward reason for this is the about 4-fold higher degree of polymerization of C_6S_{32} (N = 172.8) compared to $C_{11}S_{14}$ (N = 44.0).

Thus, the creation of a single unspecific binding site in a core–shell polymer requires a minimum degree of polymerization

Table 2 Results from Scatchard plot analyses of C_6 and C_{11} polymers

k	C_6S_{32}	$C_{11}S_{14}$
$K_{D,k}$ [μM]	28.82 ± 2.57	2.42 ± 0.35
$N_{L,MM,k}$	0.0684 ± 0.0079	0.0445 ± 0.0080
$N_{L,k}$	11.82 ± 1.37	1.96 ± 0.35

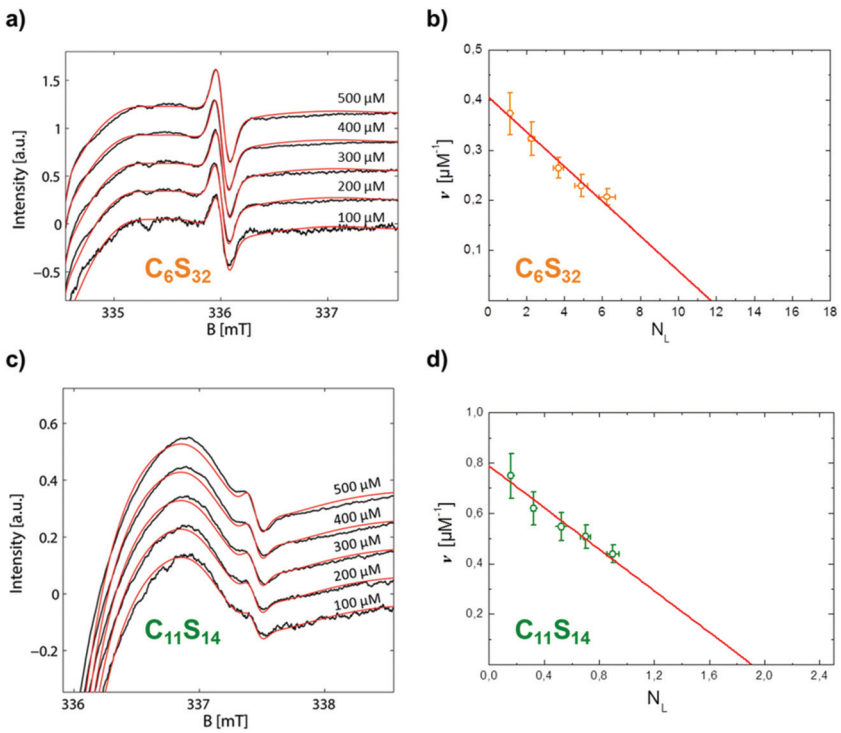

Fig. 5 Scatchard plot construction of C_6S_{32} and $C_{11}S_{14}$ loaded with 16-DSA in the nominal concentration range of 100–500 μM. The polymer concentration was 4 wt% each, *i.e.* 85 μM (C_6S_{32}) and 622 μM ($C_{11}S_{14}$). The most sensitive spectral parts of CW EPR spectra in the high-field range (335–338 mT) are highlighted. (a) All experimental CW EPR spectra (black) from 16-DSA loading of C_6S_{32} with simulations (red). (b) Scatchard plot of C_6S_{32} from (a) with linear fit according to eqn (2) (red). (c) All experimental CW EPR spectra (black) from 16-DSA loading of $C_{11}S_{14}$ with simulations (red). (d) Scatchard plot of $C_{11}S_{14}$ from (c) with linear fit (red).

of about $1/N_{L,MM,k}$ = 14–22 macromonomers containing C_6 or C_{11}-spacers, relatively unaffected by spacer length. The fifth tunable functional parameter of the core–shell polymers is therefore the number of equivalent unspecific longitudinal ligand binding sites $N_{L,k}$ per polymer, controlled by the degree of polymerization N.

2.5. Transmission electron microscopy (TEM)

For a larger-scale, yet nanoscopic, view on the polymers we applied transmission electron microscopy (TEM). Although being of a size close to the resolution limit, all types of alkylene spacer-based core–shell polymers (C_3S_{16}, C_6S_{32}, $C_{11}S_{14}$) could be visualized after staining with uranyl acetate. Fig. 6 shows soft worm-like fiber (aggregates) with diameters between 1.5 and 2.5 nm for C_3S_{16} (a), C_6S_{32} (b), and $C_{11}S_{14}$ (c) assumed to be correspondent to the approximate hydrophobic core diameter. Due to the high polymer concentration and the flexibility of the fiber (aggregates), individual fibers are difficult to resolve in full length since they may partly lie on top of each other.

Aggregated fibers with diameters of about 5 nm could be visualized by cryoEM for C_6S_{32} (Fig. S12†). However, individual fibers are too small in size and too low in contrast to be visualized in detail by the cryoEM technique. Despite the low resolution of the TEM images, we can conclude from the shapes in the images that we encounter arbitrary, chain-like structures unlike the proposed unimolecular micelle picture for such polymers given in similar studies.[16,66] We have to assume that for each core–shell polymer there is an ensemble of lower order aggregates, unimolecular micelles and chains at all temperatures with varying fractional occupations as also our DLS data exhibit partial polydisperse features especially for C_3S_{32} and $C_{11}S_{14}$ at low temperatures and C_6S_{32} at high temperatures (Fig. S8†).

2.6. Duality principle of fatty acid immobilization – proposal of the physical origin

The bimodal hydrophobic ligand immobilization we observed for C_6S_{32} and $C_{11}S_{14}$ has also been detected for the physiological transporter molecule albumin[67] and throughout literature it is considered as a ligand activation process in the substrate transporter molecule or a dynamic activation based on mutual interference and cooperation. The exact mechanism of fatty acid binding to a hydrophobic transport protein still remains somewhat enigmatic,[18,68] but is thought to be of a stepwise nature[69] as *e.g.* for cell entry.[70–72] A vast amount of EPR spectroscopic studies have elucidated lipid, steroid and fatty acid dynamics in model membranes exhibiting lateral diffusion[73–76] appearing among the principal physical phenomenon of jump diffusion first detected in pure water and lead.[77–79] Several statistical mechanic considerations regarding rotational reorientation using the solution of the angular diffusion equation[80–82] lead to practical mathematical relationships to discern between Brownian diffusion, free diffusion, and jump diffusion.[34,81,83] We observed two bound spectral fractions $F_{i,j,k}(B)$, namely b_1 and b_2, for polymers C_6S_{32} and $C_{11}S_{14}$ (Fig. 3). The rotational correlation times τ_c of b_1 and b_2 differ by a factor of 2.41 ± 0.21 (C_{11}) and 3.42 ± 0.50 (C_6) in the whole observable temperature range. Jump diffusion can be excluded to appear in our polymer system, as we deal with spatially more separated fatty acid molecules appearing neither in crowded systems as micelles, nor in a membrane bilayer. The two remaining diffusion types, Brownian diffusion and free diffusion, are considered to be most suitable to fit into polymer bound fatty acid species, as the isotropic hyperfine coupling constant a_{iso} was determined to be the same for b_1 and b_2. If 16-DSA, being attached to the polymer with the alkylene tail, underwent jump diffusion, displacements out of the polymer inside bulk water would give rise to a detectable polar spin probe environment as monitored by an increase of a_{iso}. So, we assume a spontaneous displacement of the arbitrary molecular rotation angle ψ for free diffusion, while 16-DSA still remains attached to the polymer backbone. Especially, the reorientational model parameter B_2 for slow motional EPR spectra introduced by Freed and coworkers[81] separates Brownian diffusion from free diffusion by a factor of $7^{\frac{1}{2}} \approx 2.65$.[34,84] This is surprisingly close to the observed differences in τ_c from subspectra b_1 and b_2. Moreover, the reorientational model parameter B_2 is only explicitly determined for spherically symmetric rotation. On a very fundamental level of argumentation the intrinsic axial anisotropy in 16-DSA rotation might be responsible for small deviations from the

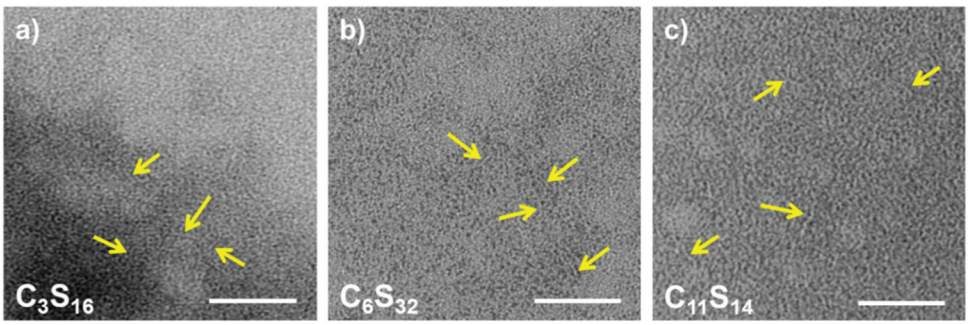

Fig. 6 TEM images of negatively stained core–shell polymers (a) C_3S_{16} , (b) C_6S_{32} and (c) $C_{11}S_{14}$. Yellow arrows point to fiber (aggregates) with diameters of a single polymer chain. The concentration for all polymers was set to 2 mg ml^{-1}. Scale bars: 50 nm.

theoretical value of 2.65 in polymers C_6S_{32} and $C_{11}S_{14}$. A further hint indicating free diffusion is given in Fig. 4a and b, as the hydrophilic collapse of the polymer shell has the shape of a sigmoidal decrease in the –log τ_c curve, but only in subspectrum b_2 of polymer C_6S_{32}. The contraction or collapse of the linear polyglycerol chains leads to a decreased local fluidity and therefore an increased local viscosity of the 16-DSA environment. This is only possible if 16-DSA in the rotational regime b_2 intercalates at the interface of hydrophobic core and hydrophilic shell, which allows the spin probe dynamics to be influenced by the shell due to its close contact. In summary, the most reasonable physical basis of this dynamic hydrophobic interconversion process is a temperature induced switching of Brownian rotational diffusion towards free diffusion of bound 16-DSA indirectly reflecting the structural integrity and self-assembling features of the individual fatty acid-bearing polymer chains by the varying spectral fractions $\phi_{b,j,k}$, while the temperature development of this process in C_6S_{32} and $C_{11}S_{14}$ is almost identical (Fig. 3d, with a shift along y-axis). An elementary model for this dynamic hydrophobic interconversion of fatty acids is given in the conclusion.

2.7. Tunable structure and dynamics of the core-shell polymers

We have revealed a wide variety of dynamic features based on the temperature dependence of the structure-based polymer–ligand and polymer–polymer interactions. In the combined picture of EPR and DLS we find that an increased ligand uptake takes place for the collapsed shell of the S_{32} polymers (Fig. 7a), C_3S_{32} and C_6S_{32}, as binding gets stronger or is facilitated with increasing temperature, most probably due to a truncated $\langle r^2 \rangle$ diffusion distance from bulk water to the hydrophobic core. This can be seen as a decreasing stealth property of the hydrophilic shell with temperature. In case of high temperature aggregation (C_6S_{32}), the hydrophobic cores are additionally shielded and ligand binding is less probable, or ligands might even be expelled from the polymeric interior for sterical reasons. To highlight the polymer-based inherent dynamics of ligand binding, we characterize this complex behavior in general as "dynamic hydrophobic interconversion" (K_{AB}) for the interconversion of rotational regimes A (b_1) to B (b_2) with the rate constants k_1 and k_{-1} and the process of ligand binding as "dynamic hydrophobic binding" (K_D) with the rate constants k_2 and k_{-2} (Fig. 7b). Together with the process of "dynamic hydrophobic aggregation" as an intermolecular feature for all polymers (Fig. 4c), we summarize these processes in terms of "dynamic hydrophobic attachment". A mathematical treatment of the resulting thermodynamics is beyond the scope of this work and is currently work in progress in our group.

The bigger such a hydrophobic core is designed relative to the hydrophilic shell, the smaller the dissociation constant K_D and the stronger the ligand binding. In Fig. 7c we depict the a_{iso}-values from our rigorous simulations of EPR spectra at 25 °C (see also Fig. S7†).

A clear decrease of a_{iso} compared to the water-exposed spin probe 16-DSA (added as C_0) is achieved upon binding to C_6 and C_{11} polymers, and the lower a_{iso}, the more nonpolar and water-depleted the hydrophobic core appears. The a_{iso}-value of the 16-DSA spin probe freely tumbling in the C_3 polymer solution is also depicted for completeness. Only at high temperatures the spin probe tends to evade exposition to the solvent by encapsulating into the small collapsed hydrophobic cores within a gel-like polymeric state, but only after the hydrophilic collapse has occurred and the hydrophobic core together with the collapsed shell forms a polymer-rich, water-separated microenvironment. Especially, the C_6S_{32} polymer displays interesting functional aspects, which can be described in the framework of a temperature induced functional activation as a ligand uptake optimum is emerging between 35 and 50 °C therefore encompassing mammalian body temperature. Furthermore, we claim that a minimum hydrophobic spacer length is necessary to facilitate uptake of fatty acid molecules in the core–shell structure at room temperature, otherwise the

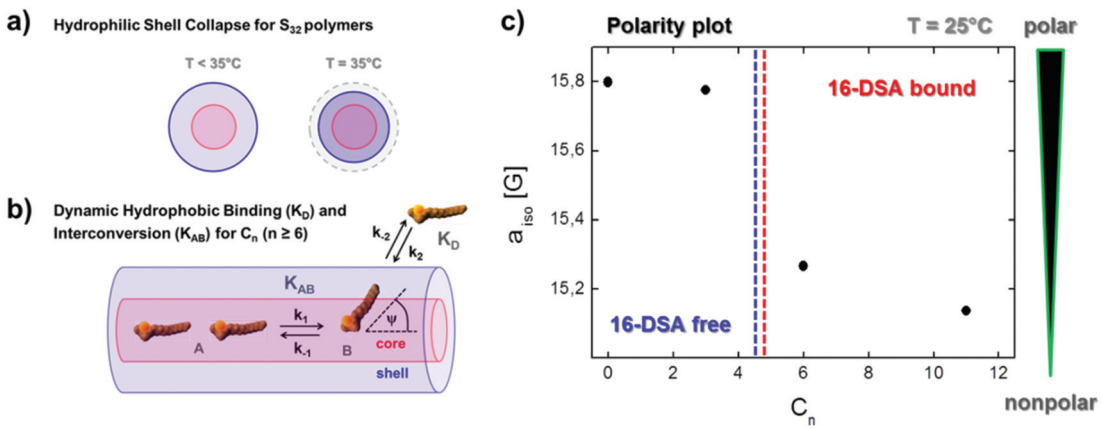

Fig. 7 Physical basis for the dynamic hydrophobic attachment principle. (a) Sketch of the hydrophilic shell collapse as monitored for S_{32} polymers. (b) Depiction of dynamic hydrophobic binding and interconversion by means of the kinetic models for K_D and K_{AB}. (c) Polarity plot of the alkylene spacer length C_n *versus* hydrophobicity by means of a_{iso} at 25 °C as probed by 16-DSA.

core is invisible for the ligand, cloaked by the hydrophilic polyglycerol shell. This critical uptake spacer length is somewhere between the C_3 and C_6 alkylene subunits in the chains. The overall uptake capability per chain can simply be adjusted by the degree of polymerization (N).

We have not tested how functionality might also depend on concentration, for both ligand and polymer. Instead, for EPR studies we restricted ourselves to polymer and fatty acid ligand concentration ranges (several hundred μM) that are in the approximate range of the native concentration of the transport protein albumin in mammalian blood.[18] This is an approach that is justified when considering such core–shell polymeric systems as protein-analogous transporters for drug delivery purposes. In similarity to often used polyethylene glycol (PEG) chains, the hydrophilic polyglycerol shell appears similar to water from a spectroscopic point of view, but reveals an indirect intricate effect upon chain and structural dynamics which might induce stealth properties to the hydrophobic cores of the polymers. This proposed stealth effect of the hydrophilic shell may even be too strong for the smaller hydrophobic cores of the C_3S_{32} polymer so that no ligand uptake may occur regularly. This is also important for their potential use as drug transporting vehicles, as the stealth effect on the one hand is promising to enhance circulation times as a polysaccharide analogue[9] while on the other hand the water-depleted core regions need to be intact and ligand migration from the core to the shell and the outside must be possible (and *vice versa* for, *e.g.*, sensor-based applications). All this is excellently fulfilled in the modular core–shell type polymers presented in this study.

One of the hallmarks of the hydrophobic effect is the linear dependence of the increased surface area with transfer free energies when dissolving linear alkylene chains in solvents.[85,86] In contrast, from our data it is apparent that the studied systems consisting of the polymerized macromonomers display a much more complicated cooperative interplay than single alkylene chains of varying length. For these albumin-analoguous polymers, the structural and dynamic parameters facilitating the imitation of protein-like behavior, as it has been shown in this study, are therefore much more difficult to assess.

From a physical methods point of view, an outstanding feature of using the nitroxide probing the dynamic molecular environment is the possibility to obtain an in depth functional view of a protein or polymer and the ligand itself without any other influences that might alter the results.[64] A few other aspects could be clarified by complementary investigations regarding dynamic self-association and shape by TEM, DLS and molecular modeling. Especially TEM showed that we have rather elongated structures than spherical collapsed micellar structures (unimolecular micelles). The clear disadvantage of our EPR approach is the incapability of reversibility studies for increasing alkylene spacer length and the complexity of the spectral simulations, which should be partly overcome with the detailed guideline to rigorous spectroscopic analysis given in this paper and corresponding ESI.†

Although many of the functional principles may be intuitive, we here establish a CW EPR-based method for a reliable and complete quantitative dynamic molecular analysis of the core–shell polymers and their ligands and found remarkable implications and conclusions for several design principles. Our findings suggest a sum of tunable, functional parameters for the core–shell polymers:

(i) We have observed three structural tuning parameters namely alkylene spacer length (C_n), the length of the hydrophilic shell (S_m) and the degree of polymerization (N) of the macromonomers. These can largely be controlled by thorough and careful synthesis and subsequent polymer characterization (see also Experimental section and ESI†).[7,9] This opens an elegant way to tailor-make polymers for delivery and uptake purposes by design and prior knowledge. Moreover, we found several dynamic properties that can be adjusted by chemical alteration of the core–shell structure.

(ii) The dynamic hydrophobic interconversion process of fatty acid species A (b_1) and B (b_2) can be designed by adjustment of C_n spacer length. This interconversion process (Fig. 3d) apparently introduces an optimum working temperature by a dynamic population crossing or transition of A and B for the polymer with optimum ligand uptake. It is influenced by intermolecular interactions like polymeric self-association as well as by intramolecular interactions as the accessibility of the hydrophobic core determined by the dynamics and size of the hydrophilic shell. This functional principle can be regarded as being the *first dynamic tuning parameter*. However, a thermodynamic model for this interconversion process has yet to be developed.

(iii) A long polyglycerol chain may lead to a hydrophilic collapse of the outer shell of the full polymer chain. This is the only dynamic effect that can be conditionally associated with the S_m chain but not directly to its length alone but rather towards the ratio of shell size (S_m) and core size (C_n). We assume a slight stealth effect of the hydrophilic shell to shield the hydrophobic core. This can be regarded as the *second dynamic tuning parameter* of the core–shell structures, and may also comprise a phase transition from a loose to a more compact structure of the polymer as also seen from DLS data. This hydrophilic collapse and stealth effect may further impose the onset of an aggregation process (C_6S_{32}) or the onset of ligand binding in a gel-like state (C_3S_{32}) to the system.

(iv) The intermolecular temperature-induced dynamic hydrophobic aggregation behavior of the polymers is found to be strongly connected to the degree of polymerization. Although implications are weak from EPR itself this is considered to be the *third dynamic tuning parameter* as confirmed by DLS data.

(v) The affinity of a ligand molecule to its binding substrate is determined by its macroscopic $K_{D,k}$ value as it can be extracted from *e.g.* Scatchard plots. By increasing alkylene spacer length (C_n) the $K_{D,k}$ value can be adjusted within orders of magnitude. The adjustment of the dynamic hydrophobic binding affinity towards a ligand molecule is the *fourth dynamic tuning parameter* of the core–shell polymers.

(vi) The degree of polymerization (N) is the decisive parameter for how many ligands can be bound to unspecific ligand binding sites per polymer ($N_{L,k}$), as an increase of the alkylene spacer length (C_n) does not necessarily improve the number of bound ligands per macromonomer ($N_{L,MM,k}$). This is also indicative for a longitudinal alignment of the bound ligands and is regarded as the *fifth dynamic tuning parameter* affected by the structure of the core–shell polymer. Partial aggregation behavior may furthermore alter the individual ligand binding capacity of a polymer. A single unspecific binding site is found to be constructed by polymerization of 14–22 macromonomers.

3. Conclusions

The overall characteristics of the mutual interactions of amphiphilic ligands and amphiphilic transporters is summarized as the concept of "dynamic hydrophobic attachment" as this term is to the best of our knowledge not used for any particular mechanism elsewhere. This term shall comprise an intermolecular polymeric "dynamic hydrophobic aggregation", a ligand based "dynamic hydrophobic binding" and "dynamic hydrophobic interconversion" that have been shown to react sensitively on structural changes of the core–shell substrate. Astonishingly, as we have seen from C_6S_{32} and $C_{11}S_{14}$ polymers the global rotational dynamics as monitored by τ_c do not seem to depend strongly on molecular weight of the polymer and therefore the degree of polymerization N, which simplifies comparative studies decisively. Nonetheless, the strong temperature dependence of both polymer dynamics and ligand affinity indicates suitable applications in minimally invasive surgery in terms of controlled ligand uptake and release in combination with *e.g.* LASER- or electro-hyperthermia treatment.[87] This ligand uptake is not restricted to stearic acids only, but may be extended to any amphiphilic or hydrophobic medical ingredient that can be finally subject to a targeted drug release.[64,88] In addition, the RAFT polymerization derived core–shell structures may further provide access to covalently modified telechelic structures with cleavable and non-cleavable release properties, as demonstrated in the ESI,† that enhance their applicability towards smart drug delivery purposes as well.

Although being far from complete, this study gives a blueprint for the further design and the characterization of amphiphilic core–shell structures to systematically screen ligands and hydrophobic core and hydrophilic shell structures to obtain suitable synthetic drug transporter molecules working in the scheme of dynamic hydrophobic attachment.

4. Experimental section

4.1 Materials

All C_3- and C_6-based core–shell polymers were synthesized as described in Thomas *et al.*,[9] while the C_{11}-based core–shell polymers were prepared as described in the following. Solvents and reagents were purchased from Sigma-Aldrich or Acros Organics and used without further purification, unless stated otherwise. The spin-labeled fatty acid 16-DSA (Sigma-Aldrich, Taufkirchen) was used without further purification. 1-Chloro-3-hydroxypropane was purchased from abcr, Texas Red methanethiosulfonate (Texas Red-2-sulfonamidoethyl methanethiosulfonate) was purchased from Toronto Research Chemicals and Texas Red cadaverine was obtained from Invitrogen. 2,2′-Azobis(isobutyronitrile) (AIBN) was recrystallized from diethyl ether and stored at −7 °C. Deuterated solvents were purchased from Deutero GmbH. Dialysis tubings were purchased from CelluSep (MWCO = 1000 g mol^{-1} or 25 000 g mol^{-1}) or from Carl Roth GmbH + Co. KG (Spectra/Por 3 membranes, MWCO = 8000–10 000 g mol^{-1}). Thin layer chromatography (TLC) was performed on TLC aluminium sheets (20 × 20 cm, silica gel 60 F254) purchased from Merck and methanol was used as eluent. Anhydrous THF and dioxane were freshly distilled from a sodium/potassium mixture. Azido undecanoyl methacrylate (AzUMA)[89] and 4-(4,6-dimethoxy-1,3,5-triazin-2-yl)-4-methyl morpholinium chloride (DMTMM-Cl))[90] were prepared modified to literature procedures. (4-Cyanopentanoic acid)dithiobenzoate[91] and monopropargyl-functional linear polyglycerol (*lin*PPG$_m$)[9] were prepared as described previously. Detailed experimental information and NMR spectra are given in the ESI† (see corresponding Experimental section).

4.2 Copper-catalyzed azide–alkyne cycloaddition of *lin*PPG$_m$ and AzUMA

In a typical experiment, *lin*PPG$_m$ (1 eq.) was dissolved in methanol (1 ml per 100 mg *lin*PPG) and AzUMA (1.5 eq.) and PMDETA (0.3 eq.) were added. After degassing *via* three freeze–pump–thaw cycles, CuBr (0.3 eq.) was added under argon. The solution was stirred at room temperature overnight. The reaction was stopped by exposing the catalyst to air and an acidic ion exchange resin (DOWEX 50WX8) was added to remove copper. The colorless solution was neutralized by the addition of basic ion exchange resin (Amberlite IRA67), filtered, and BHT (2.5 mg per 100 mg polymer) was added as a stabilizer. Solvents were removed under reduced pressure at room temperature and the product was stored at −27 °C to prevent premature polymerization. The crude product was precipitated in diethyl ether prior to polymerization to remove residual low molecular weight AzUMA and stabilizer. Yields were between 80% and 100% and characterization data for click-coupled macromonomers can be found in Table S3.† Furthermore, NMR data and SEC traces are given in Fig. S13–S15.†

NMR measurements. ^{1}H, ^{13}C and 2D NMR spectra were recorded using an Avance III HD 300 or an Avance II 400 spectrometer. Residual proton signals of the deuterated solvent were used as an internal reference.

^{1}H NMR (methanol-d_4, 400 MHz): δ (ppm) = 8.03 (s, 1H, triazole), 6.11 and 5.64 (m, 2H, CH_2=C), 4.81 (m, 2H, OCH_2CN), 4.43 (t, 2H, NCH_2CH$_2$, J = 7.1 Hz), 4.18 (t, 2H, CH$_2$CH_2OCO, J = 6.6 Hz), 3.82–3.50 (m, polyether backbone), 3.48 (t, 2H, CH$_3$CH$_2$CH_2O, J = 6.7 Hz), 1.98–1.89 (m, 5H, CH_3C=CH$_2$ and

NCH_2CH_2), 1.75–1.59 (m, 4H, $CH_3CH_2CH_2O$ and CH_2CH_2OCO), 1.48–1.29 (m, 14H, $NCH_2CH_2(CH_2)_7CH_2CH_2OCO$), 0.97 (t, 3H, $CH_3CH_2CH_2O$, J = 7.4 Hz).

^{13}C NMR (methanol-d_4, 100 MHz): δ (ppm) = 168.94 (C=O), 146.38 (HC=CN), 137.92 (C=CH_2), 125.94 (C=CH_2), 124.98 (HC=CN), 81.56 ($CH_2CH(CH_2OH)$), 80.61 ($CH_2CH(CH_2OH)$, terminal), 74.04 ($CH_3CH_2CH_2O$), 71.92–70.59 (CH_2 polyether backbone), 65.94 (CH_2CH_2OCO). 64.06 (OCH_2CN), 62.63 (CH_2OH), 51.38 (NCH_2CH_2), 31.32 (NCH_2CH_2), 30.53–30.08, 27.49 and 27.07 ($NCH_2CH_2(CH_2)_7CH_2CH_2OCO$), 29.69 ($CH_2CH_2OCO$), 23.88 ($CH_3CH_2CH_2O$), 18.43 ($CH_3C$=$CH_2$), 10.92 ($CH_3CH_2CH_2O$).

SEC measurements. The measurements were performed in DMF containing 0.25 g L^{-1} of lithium bromide (LiBr) as an additive on an Agilent 1100 Series instrument, including a PSS HEMA column (300/100/40), an UV (275 nm), and a RI detector. Calibration was carried out using poly(ethylene oxide) standards provided by Polymer Standards Service (PSS). SEC measurements of high molecular weight graft copolymers were conducted in DMF (containing 1.0 g L^{-1} LiBr) using a PSS SecCurity (Agilent Technologies 1260 infinity) setup equipped with a PSS GRAM column (porosity: linear M; particle size: 10 μm; dimensions: 0.8 × 30 cm), a DAWN EOS (Wyatt Technology) and an RI detector.

4.3 RAFT-polymerization of click-coupled macromonomers

In a typical protocol, the macromonomer (30 eq.) was dissolved in water (1 ml per 200 mg macromonomer). (4-Cyanopentanoic acid)dithiobenzoate (CTA, 1 eq.) and AIBN (0.2 eq.) were dissolved in freshly distilled dioxane and added to the macromonomer solution to yield a water/dioxane ratio of 9 : 1. The solution was degassed *via* three freeze–pump–thaw cycles and the polymerization was performed for 48–72 h at 65 °C. The reaction was stopped by exposing the solution to air and the solvents were removed under reduced pressure. The residue was dissolved in methanol and precipitated in cold diethyl ether or dialyzed against water (MWCO = 25 000).

Yields were at ~50% and characterization data for graft copolymers P(*lin*PGTzUMA) are given in Table S4 and Fig. S16–S20 in the ESI.† Moreover, further details on the post polymerization endgroup modification towards heterotelechelic graft copolymers can be found in Fig. S21–S24.† Additional information about synthesis of DMTMM-Cl is given in Scheme S3 as well as Fig. S25 and S26.†

NMR measurements. ^{1}H NMR (DMSO-d_6, 400 MHz): δ (ppm) = 8.03 (s, 1H, triazole), 4.71–4.45 (m, OCH_2C=C and OH), 4.29 (br, 2H, NCH_2CH_2), 3.93–3.12 (m, polyether backbone), 1.54–1.45 (m, $CH_3CH_2CH_2O$), 0.85 (t, 3H, $CH_3CH_2CH_2O$, J = 7.4 Hz), 1.87–0.75 ($NCH_2(CH_2)_9CH_2OCO$, and polymethacrylate backbone).

^{13}C NMR (DMSO-d_6, 100 MHz): δ (ppm) = 144.61 (HC=CN), 123.49 (HC=CN), 80.14–79.90 ($CH_2CH(CH_2OH)$), 79.05–78.84 ($CH_2CH(CH_2OH)$, terminal), 71.97 ($CH_3CH_2CH_2OCH_2$), 70.63 and 70.15 ($PrOCH_2CH_2O$ and $PrOCH_2CH_2OCH_2$), 69.61–69.00 (CH_2 polyether backbone), 62.76–62.60 (OCH_2CN), 61.10–60.68 (CH_2OH), 49.30 (NCH_2CH_2), 29.89 (NCH_2CH_2), 29.48–28.39, 26.23–25.45 ($NCH_2CH_2(CH_2)_7CH_2CH_2OCO$), 22.48 ($CH_3CH_2CH_2O$), 10.56 ($CH_3CH_2CH_2O$).

4.4 EPR Spectroscopy

Sample preparation. All core–shell polymers were dissolved in ultrapure water (Milli-Q) to polymer stock concentrations of 2.5–9.4 wt% corresponding to 0.2 to 1.2 mM. For adding the spinprobe molecules to the polymer samples a solution of 8 mM 16-DSA in 0.1 M KOH was prepared. The final concentrations were adjusted by adding pure water for a final sample volume of 40 μl. Due to addition of 0.1 M KOH the pH values were precautiously checked exhibiting almost neutral values from pH 7.5 ± 0.5. As a reference standard we also conducted spectral simulations of temperature dependent solutions of 16-DSA in DPBS buffer[52] alone as given in Fig. S2.† The buffer was used to facilitate titration of the sample from an initial value of pH 9.7 (0.1 M KOH) to a physiological value of pH 7.4 by buffers with well-adjusted amounts of HCl and NaOH. About 10–15 μl of the final solutions were filled into micropipettes (BLAUBRAND intraMARK, Wertheim, Germany) and capped with capillary tube sealant (Leica CRITOSEAL) for an immediate supply to the EPR spectrometer.

EPR measurements. CW EPR spectroscopic measurements were conducted on Miniscope MS200 and MS400 (MAGNETTECH, Berlin, Germany) benchtop spectrometers at X-band microwave frequencies of about 9.4 GHz. Measurements were performed with microwave powers between 3.2 to 10.0 mW with a sweep width of 12–15 mT and a modulation amplitude of 0.1 mT. For temperature-dependent measurements a temperature controller (MAGNETTECH Temperature Controller H03) was used and the microwave frequency was recorded with a frequency counter (RACAL DANA, model 2101, Neu-Isenburg, Germany). The EPR spectra used for the temperature response curves of the polymers were recorded in steps of ΔT = 5 K from 5 to 95 °C with a precautionary incubation time for each temperature step of about 2–3 min.

EPR spectral analysis. Spectral simulations were performed exclusively in MATLAB (R2008b, v.7.7) utilizing the software package EasySpin 5.0.2.[92] All MATLAB codes have been optimized for 1–3 component CW EPR nitroxide spectra with appropriate home-written routines. In principle the individual emerging subspectra were extracted in an iterative manual procedure and double-integrated to extract the spectral fractions $\phi_{i,j,k}$ of the corresponding dynamic populations and hence conducted the reconstruction of experimental spectra $S_{j,k}(B)$. A reasonable set of simulation parameters is given in Table S1† and the simulation approach is given in detail in the ESI.†

4.5 Negative stain electron microscopy (EM)

The core–shell polymer samples were prepared in pure water to give concentrations of 0.2 wt%. Negatively stained samples were prepared by spreading 5 μL of the dispersion onto a Cu grid coated with a Formvar-film (PLANO, Wetzlar, Germany). After 1 min excess liquid was blotted off with filter paper and 5 μL of 1% aqueous uranyl acetate solution were placed onto

the grid and drained off after 1 min. Specimens were air-dried and examined in an EM 900 transmission electron microscope (Carl Zeiss Microscopy GmbH, Oberkochen, Germany). Micrographs were taken with a SSCCD SM-1k-120 camera (TRS, Moorenweis, Germany).

4.6 DLS measurements

All DLS data have been obtained by using an ALV-NIBS high performance particle sizer (HPPS) equipped with an ALV-5000/EPP Multiple Tau Digital Correlator (ALV-Laser Vertriebsgesellschaft m. b. H., Langen, Germany). This device facilitates HeNe-LASER irradiation with a typical wavelength of λ = 632.8 nm and 3 mW output power with an automatic attenuator for optimum count rates recorded in a backscattering setup detection angle of 173° relative to the incident monochromatic light. The sample cell temperatures were adjusted in the range of 8–85 °C in steps of 3 to 4 K by a Peltier temperature control unit. All samples have been prepared with a polymer concentration of 0.13–0.20 wt% (4.3–20.7 μM) and have been measured in 1.5 ml PMMA semi-micro cuvettes (BRAND, Wertheim). For sustaining comparability, a 1 mM 16-DSA stock solution in 12.5 mM KOH was used to equip the polymers with the same fatty acid loading as for the EPR measurements in this case well below the critical micelle concentration. The polymer concentrations were adjusted with ultrapure water (Milli-Q) to a final sample volume of 400–600 μl giving slightly alkaline solutions at about pH 8.1. All samples were filtered through Rotilabo cellulose acetate (CA) syringe filters with a pore size of 0.2 μM (CARL ROTH, Karlsruhe, Germany) to minimize adhesion. Data were extracted from the intensity correlation functions by a $g_2(t)$-DLS exponential and a mass weighted regularized fit in the ALV-NIBS software v.3.0 utilizing the CONTIN algorithm.[55] While the refractive index was assumed to be constant at n_{H_2O} = 1.332 for all temperatures, the water viscosity was corrected for each temperature. Each sample was measured at least 4 times at the same temperature for 60 s and was averaged at least over three individual values. The mean values $R_{H,j,k}$ of the most prominent particle size peaks and their statistical fluctuations are given as the standard deviation as depicted in the error bars in Fig. 4b. The duration of a heating procedure was 8–12 h. The temperature dependent size distributions are given in Fig. S8† as indicated in the main text.

4.7 Molecular dynamics (MD) simulations

All molecular models of the coreshell-polymers were constructed using the YASARA-structure software.[93] The MD simulations were run in simulation boxes with periodic cell boundaries containing the polymer and an explicit water solvent with 370 000–403 000 atoms in total. The simulation runtime was 12–13 ns at pH 7.0 in 0.0 M NaCl and T = 298 K applying the AMBER03 forcefield. Due to calculational effort, the model sizes were limited to a molecular weight of 100 kDa (N = 32–37) and are therefore only consulted for generalized phenomenological conclusions.

Acknowledgements

We gratefully acknowledge helpful discussions with Dr. Andreas Kerth and Dr. Christian Schwieger (both MLU Halle-Wittenberg) and Prof. Dr. Rudolf Zentel (JGU Mainz). We are also grateful to Dr. Gerd Hause (Microscopy Unit, Biocenter, MLU Halle-Wittenberg) for recording the cryoTEM image, Christine Rosenauer (MPI for Polymer Research, Mainz) for SEC-MALLS measurements, and to Heike Schimm and Stefanie Weber for continuing technical support. This work was financially supported by the Deutsche Forschungsgemein-schaft (DFG) under grant number HI 1094/5-1 and by the Max Planck Graduate Center with the Johannes Gutenberg-University Mainz (MPGC).

Notes and references

1 X. S. Wang, S. F. Lascelles, R. A. Jackson and S. P. Armes, *Chem. Commun.*, 1999, **18**, 1817.
2 X. S. Wang and S. P. Armes, *Macromolecules*, 2000, **33**, 6640.
3 M. Zhang, T. Breiner, H. Mori and A. H. E. Müller, *Polymer*, 2003, **44**, 1449.
4 B. H. Tan, H. Hussain, Y. Liu, C. B. He and T. P. Davis, *Langmuir*, 2009, **26**, 2361.
5 Y. Y. Yuan, Q. Du, Y. C. Wang and J. Wang, *Macromolecules*, 2010, **43**, 1739.
6 C. Porsch, S. Hansson, N. Nordgren and E. Malmström, *Polym. Chem.*, 2011, **2**, 1114.
7 A. Thomas, F. K. Wolf and H. Frey, *Macromol. Rapid Commun.*, 2011, **32**, 1910.
8 Y. L. Luo, W. Yu, F. Xu and L. L. Zhang, *Polym. Chem.*, 2012, **50**, 2053.
9 A. Thomas, K. Niederer, F. Wurm and H. Frey, *Polym. Chem.*, 2014, **5**, 899.
10 J. F. Lutz, *J. Polym. Sci., Part A: Polym. Chem.*, 2008, **46**, 3459.
11 J. F. Lutz, *Adv. Mater.*, 2011, **23**, 2237.
12 F. Herbst, D. Döhler, P. Michael and W. H. Binder, *Macromol. Rapid Commun.*, 2013, **34**, 203.
13 D. Döhler, P. Michael and W. H. Binder, in *Self-Healing Polymers: From Principles to Applications*, ed. W. H. Binder, Wiley-VCH, Weinheim, Germany, 2013, pp. 5–60.
14 J. Z. Du, L. Y. Tang, W. J. Song, Y. Shi and J. Wang, *Biomacromolecules*, 2009, **10**, 2169.
15 O. G. Schramm, M. A. R. Meier, R. Hoogenboom, H. P. van Erp, J. F. Gohy and U. S. Schubert, *Soft Matter*, 2009, **5**, 1662.
16 J. A. Johnson, Y. Y. Lu, A. O. Burts, Y. H. Lim, M. G. Finn, J. T. Koberstein, N. J. Turro, D. A. Tirrell and R. H. Grubbs, *J. Am. Chem. Soc.*, 2010, **133**, 559.
17 Y. Bakkour, V. Darcos, F. Coumes, S. Li and J. Coudane, *Polymer*, 2013, **54**, 1746.
18 T. Peters Jr., *All about Albumin: Biochemistry, Genetics, and Medical Applications*, Academic Press, San Diego, 1995.

19 S. J. Rehfeld, D. J. Eatough and W. Z. Plachy, *J. Lipid Res.*, 1978, **19**, 841.
20 R. C. Perkins Jr., N. Abumrad, K. Balasubramanian, L. R. Dalton, A. H. Beth, J. H. Park and C. R. Park, *Biochemistry*, 1982, **21**, 4059.
21 T. G. Gantchev and M. B. Shopova, *Biochim. Biophys. Acta, Protein Struct. Mol. Enzymol.*, 1990, **1037**, 422.
22 M. Ge, S. B. Rananavare and J. H. Freed, *Biochim. Biophys. Acta, Gen. Subj.*, 1990, **1036**, 228.
23 M. J. N. Junk, H. W. Spiess and D. Hinderberger, *Angew. Chem., Int. Ed.*, 2010, **49**, 8755.
24 J. Reichenwallner and D. Hinderberger, *Biochim. Biophys. Acta, Gen. Subj.*, 2013, **1830**, 5382.
25 Y. Akdogan, Y. Wu, K. Eisele, M. Schaz, T. Weil and D. Hinderberger, *Soft Matter*, 2012, **8**, 11106.
26 S. L. Kuan, B. Stöckle, J. Reichenwallner, D. Y. Ng, Y. Wu, M. Doroshenko, K. Koynov, D. Hinderberger, K. Müllen and T. Weil, *Biomacromolecules*, 2013, **14**, 367.
27 D. Kurzbach, D. R. Kattnig, B. Zhang, A. D. Schlüter and D. Hinderberger, *Chem. Sci.*, 2012, **3**, 2550.
28 D. Kurzbach, W. Hassouneh, J. R. McDaniel, E. A. Jaumann, A. Chilkoti and D. Hinderberger, *J. Am. Chem. Soc.*, 2013, **135**, 11299.
29 D. Kurzbach, M. N. Reh and D. Hinderberger, *ChemPhysChem*, 2011, **12**, 3566.
30 D. Kivelson, *J. Chem. Phys.*, 1960, **33**, 1094.
31 J. H. Freed and G. K. Fraenkel, *J. Chem. Phys.*, 1963, **39**, 326.
32 J. H. Freed, *J. Chem. Phys.*, 1964, **41**, 2077.
33 T. J. Stone, T. Buckman, P. L. Nordio and H. M. McConnell, *Proc. Natl. Acad. Sci. U. S. A.*, 1965, **54**, 1010.
34 J. H. Freed, in *Spin Labeling: Theory and Applications*, ed. L. J. Berliner, Academic Press, New York, 1976, vol. 1, pp. 53–132.
35 W. L. Hubbell and C. Altenbach, *Curr. Opin. Struct. Biol.*, 1994, **4**, 566.
36 O. H. Griffith, P. J. Dehlinger and S. P. Van, *J. Membr. Biol.*, 1974, **15**, 159.
37 H. J. Steinhoff, A. Savitzky, C. Wegener, M. Pfeiffer, M. Plato and K. Möbius, *Biochim. Biophys. Acta, Bioenerg.*, 2000, **1457**, 253.
38 G. Moad, E. Rizzardo and S. H. Thang, *Aust. J. Chem.*, 2005, **58**, 379.
39 G. Moad, Y. K. Chong, A. Postma, E. Rizzardo and S. H. Thang, *Polymer*, 2005, **46**, 8458.
40 G. Moad, E. Rizzardo and S. H. Thang, *Polymer*, 2008, **49**, 1079.
41 O. H. Griffith and A. S. Waggoner, *Acc. Chem. Res.*, 1969, **2**, 17.
42 D. A. Windrem and W. Z. Plachy, *Biochim. Biophys. Acta, Biomembr.*, 1980, **600**, 655.
43 D. Hinderberger, in *EPR Spectroscopy: Applications in Chemistry and Biology*, ed. M. Drescher and G. Jeschke, Springer, Berlin, Heidelberg, 2012, pp. 67–89.
44 A. S. Waggoner, T. J. Kingzett, S. Rottschaefer, O. H. Griffith and A. D. Keith, *Chem. Phys. Lipids*, 1969, **3**, 245.
45 J. Reichenwallner, C. Schwieger and D. Hinderberger, unpublished work.
46 M. J. N. Junk, W. Li, A. D. Schlüter, G. Wegner, H. W. Spiess, A. Zhang and D. Hinderberger, *Angew. Chem., Int. Ed.*, 2010, **49**, 5683.
47 N. C. Pace and C. Tanford, *Biochemistry*, 1968, **7**, 198.
48 A. V. Finkelstein and O. B. Ptitsyn, *Protein physics: a course of lectures*, Academic Press, London, San Diego, 2002.
49 M. J. N. Junk, U. Jonas and D. Hinderberger, *Small*, 2008, **4**, 1485.
50 M. J. N. Junk, W. Li, A. D. Schlüter, G. Wegner, H. W. Spiess, A. Zhang and D. Hinderberger, *Macromol. Chem. Phys.*, 2011, **212**, 1229.
51 D. Kurzbach, M. J. N. Junk and D. Hinderberger, *Macromol. Rapid Commun.*, 2013, **34**, 119.
52 R. Dulbecco and M. Vogt, *J. Exp. Med.*, 1954, **99**, 167.
53 C. Tanford, *J. Mol. Biol.*, 1972, **67**, 59.
54 W. J. Simmonds, *Aust. J. Exp. Biol. Med. Sci.*, 1972, **50**, 403.
55 S. W. Provencher, *Comput. Phys. Commun.*, 1982, **27**, 229.
56 P. R. Majhi and A. Blume, *J. Phys. Chem. B*, 2002, **106**, 10753.
57 P. J. Tummino and R. A. Copeland, *Biochemistry*, 2008, **47**, 5481.
58 J. F. W. Keana, in *Spin labeling: Theory and applications*, ed. L. J. Berliner, Academic Press, New, York, 1979, vol. 2, pp. 115–172.
59 Y. Ma, C. Loyns, P. Price and V. Chechik, *Org. Biomol. Chem.*, 2011, **9**, 5573.
60 E. A. Haidasz, D. Meng, R. Amorati, A. Baschieri, K. U. Ingold, L. Valgimigli and L. A. Pratt, *J. Am. Chem. Soc.*, 2016, **138**, 5290.
61 R. A. Copeland, *Enzymes: A Practical Introduction to Structure, Mechanism, and Data Analysis*, Wiley-VCH, New York, 2000.
62 G. Scatchard, *Ann. N. Y. Acad. Sci.*, 1949, **51**, 660.
63 C. Tanford, *Physical Chemistry of Macromolecules*, John Wiley & Sons, New York, 1961.
64 T. Hauenschild, J. Reichenwallner, V. Enkelmann and D. Hinderberger, *Chem. – Eur. J.*, 2016, **22**, 12825–12838.
65 J. Matsui, Y. Miyoshi, O. Doblhoff-Dier and T. Takeuchi, *Anal. Chem.*, 1995, **67**, 4404.
66 H. Hussain, K. Y. Mya and C. He, *Langmuir*, 2008, **24**, 13279.
67 A. Gurachevsky, E. Shimanovitch, T. Gurachevskaya and V. Muravsky, *Biochem. Biophys. Res. Commun.*, 2007, **360**, 852.
68 J. A. Hamilton, *Prog. Lipid Res.*, 2004, **43**, 177.
69 W. Scheider, *J. Phys. Chem.*, 1980, **84**, 925.
70 F. Kamp and J. A. Hamilton, *Prostaglandins, Leukotrienes Essent. Fatty Acids*, 2006, **75**, 149.
71 J. A. Hamilton, *Prostaglandins, Leukotrienes Essent. Fatty Acids*, 2007, **77**, 355.
72 E. Barta, *J. Membr. Biol.*, 2015, **248**, 783.
73 E. Sackmann and H. Träuble, *J. Am. Chem. Soc.*, 1972, **94**, 4482.

74 E. Sackmann and H. Träuble, *J. Am. Chem. Soc.*, 1972, **94**, 4492.
75 C. J. Scandella, P. Devaux and H. M. McConnell, *Proc. Natl. Acad. Sci. U. S. A.*, 1972, **69**, 2056.
76 H. Träuble and E. Sackmann, *Nature*, 1973, **245**, 210.
77 B. N. Brockhouse, *Il Nuovo Cimento*, 1958, **9**, 45.
78 B. N. Brockhouse and N. K. Pope, *Phys. Rev. Lett.*, 1959, **3**, 259.
79 C. T. Chudley and R. J. Elliott, *Proc. Phys. Soc.*, 1961, **77**, 353.
80 P. A. Egelstaff, *J. Chem. Phys.*, 1970, **53**, 2590.
81 S. A. Goldman, G. V. Bruno, C. F. Polnaszek and J. H. Freed, *J. Chem. Phys.*, 1972, **56**, 716.
82 K. A. Valiev and E. N. Ivanov, *Phys. Usp.*, 1973, **16**, 1.
83 G. V. Bruno and J. H. Freed, *J. Phys. Chem.*, 1974, **78**, 935.
84 K. A. Earle, D. E. Budil and J. H. Freed, *J. Phys. Chem.*, 1993, **97**, 13289.
85 K. A. Sharp, A. Nicholls, R. F. Fine and B. Honig, *Science*, 1991, **252**, 106.
86 I. Tunon, E. Silla and J. L. Pascual-Ahuir, *Protein Eng.*, 1992, **5**, 715.
87 H. Sahinbas, D. H. W. Grönemeyer, E. Böcher and A. Szasz, *J. Ger. Oncol.*, 2007, **39**, 1.
88 R. Haag, *Angew. Chem., Int. Ed.*, 2004, **43**, 278.
89 Q. Shen, J. Zhang, S. Zhang, Y. Hao, W. Zhang, W. Zhang, G. Chen, Z. Zhang and X. J. Zhu, *Polym. Sci., Part A: Polym. Chem.*, 2012, **50**, 1120.
90 M. Kunishima, C. Kawachi, F. Iwasaki, K. Terao and S. Tani, *Tetrahedron Lett.*, 1999, **40**, 5327.
91 L. Nuhn, M. Hirsch, B. Krieg, K. Koynov, K. Fischer, M. Schmidt, M. Helm and R. Zentel, *ACS Nano*, 2012, **6**, 2198.
92 S. Stoll and A. Schweiger, *J. Magn. Reson.*, 2006, **178**, 42.
93 E. Krieger, T. Darden, S. B. Nabuurs, A. Finkelstein and G. Vriend, *Proteins: Struct., Funct., Bioinf.*, 2004, **57**, 678.